INTERNATIONAL JOURNAL FOR NUMERICAL METHODS IN FLUIDS
Int. J. Numer. Meth. Fluids 2006; **50**:947–972
Published online 31 October 2005 in Wiley InterScience (www.interscience.wiley.com). DOI: 10.1002/fld.1089

Adjoint approach of the spatial sensitivity to disturbances of internal flows with free surface

O. Bouizi[‡] and C. Delcarte[*,†]

Université Paris-Sud XI, LIMSI-CNRS, B.P. 133, 91403 Orsay, Cedex, France

SUMMARY

A local adjoint technique is developed in order to determine the most sensitive location to perturbations of steady states near bifurcation points in the case of confined flows with free-surface boundary. Transitions to stationary or periodic flows are studied. The method is validated by comparison of its results with those given by a time approach. It is then applied to the stability study and the feedback control of thermocapillary flows in liquid bridge. Copyright © 2005 John Wiley & Sons, Ltd.

KEY WORDS: adjoint method; collocation spectral method; flow stability; thermocapillary convection

1. INTRODUCTION

Recent years have seen growing interest in flow control as well as in experimental works as in numerical studies. Sensitivity analysis has been applied in a large number of research areas such as uncertainty analysis [1], aerodynamic design optimization [2, 3], parameter estimation [4], data assimilation [5] and inverse heat conduction problem [6]. The use of adjoint equations in optimal control theory was first performed by Lions [7]. Introduced in fluid dynamics by Pironneau [8] in 1974, it has been intensively used in aerodynamic shape design [2, 9–11] and optimal error control [12]. In all of these numerical studies, the heart of the method is an optimization procedure which uses an adjoint approach to compute the linear sensitivity of an objective function with respect to a number of variables.

Hill [13] developed a local adjoint technique to study the influence of inhomogeneous wall conditions and source terms in exciting two-dimensional Tollmien-Schlichting waves in the Blasius flow. A similar nonlocal technique was then applied by Luchini and Bottaro [14] in the case of Görtler vortices developing over a concave wall boundary layer and on the receptivity of the boundary layer produced by the impulsive motion of a flat plate in its plane [15]. The receptivity analysis here is based on the upstream integration of the adjoint equations at

*Correspondence to: C. Delcarte, Université Paris-Sud XI, LIMSI-CNRS, B.P. 133, 91403 Orsay, Cedex, France.
†E-mail: delcarte@limsi.fr, claudine.dang-vu@limsi.fr
‡E-mail: othman.bouizi@limsi.fr

Received 12 January 2005
Revised 4 August 2005
Accepted 11 August 2005

the same computational cost as a forward integration of the direct problem. Andersson *et al.* [16] calculated the optimal perturbations of a flat plate boundary layer by a similar technique. Gadoin *et al.* [17] applied the method in order to determine the location of the maximum receptivity of the boundary layer modes in a long differentially heated cavity.

The aim of the present paper is to provide a low-cost computer method, based on an adjoint approach, which is able to determine the most sensitive location to disturbances, no more in case of boundary layers flows, as in the here above-mentioned studies, but in confined flows with free-surface boundary. The applications field is then very large and, to our knowledge, unexplored till now.

The test configuration is the side-heated liquid bridge, whose stability has been widely explored [18, 19]. The motivation of the previous studies was to contribute to the understanding of the hydrodynamics of flows occurring in the floating zone crystal growth process. Indeed, experiments have shown that the oscillatory state of the thermocapillary convection flow causes detrimental striations in the chemical composition of the finished single crystal [20]. Active control was experimentally performed by installation of sensor/heater pairs on the free surface, in order to suppress the oscillations [21]. The performance of the control depends on the sensor/heater position. We shall show how our adjoint approach could help the experimenter.

This paper is organized as follows. Section 2 explains two ways to obtain the response amplitude to a disturbance: a time-dependent approach and the adjoint approach. Section 3 presents the physical test configuration and its mathematical model. The adjoint system is deduced from the linearized Navier–Stokes equations and the associated boundary conditions. Section 4 summarizes the used numerical tools. The adjoint method is validated by comparison of the amplitudes of its responses to temperature and velocity disturbances with the amplitudes given by the time approach. Several bifurcation types are tested. In Section 5, the method is applied to the study of the stability of the liquid bridge with respect to the Prandtl number values. Section 6 explains how the method can help the experimenter to control the flow. We conclude in Section 7.

2. SENSITIVITY ANALYSIS

2.1. Time-dependent approach

The linear stability study in hydrodynamics is generally based on the analysis of the eigenvalues of the operator resulting from the linearization of the Navier–Stokes equations and their boundary conditions in the domain $\mathscr{D}$. The flow field $\mathbb{U}$ is decomposed into a steady-state $\mathbb{U}_0$ and a small amplitude disturbance $\mathbb{u}$:

$$\mathbb{U} = \mathbb{U}_0 + \mathbb{u} \tag{1}$$

Substituting into the Navier–Stokes equations and the boundary conditions yields the linearized equations governing the evolution of small disturbances,

$$\frac{\partial \mathbb{u}}{\partial t} = \mathscr{L}(\mathbb{U}_0, \mathbb{u}) \tag{2}$$

with linearized boundary conditions $\mathscr{B}$. The formal solution of these equations can be written as

$$\mathbb{u} = \exp(t\mathscr{L}(\mathbb{U}_0, \mathbb{u}))\mathbb{u}_0 \tag{3}$$

with $\mathbb{u}_0$ as the initial condition. Unfortunately, the operator exponential is very seldom explicitly available. A common tool to deduce the behaviour of $\exp(t\mathscr{L}(\mathbb{U}_0, \mathbb{u}))$ consists in the calculation of characteristic values associated with Equation (2):

$$\mathscr{L}(\mathbb{U}_0, \mathbb{u}_i) = \lambda_i \mathbb{u}_i \tag{4}$$

where λ_i and $\mathbb{u}_i$ denote a particular eigenvalue and eigenvector of $\mathscr{L}$. We have assumed that there are no degeneracies and that $\mathscr{L}$ can be completely diagonalized. The dynamics of the disturbances can then be deduced from the spectrum of $\mathscr{L}$.

If the set $\mathbb{u}_i$ spans the volume $\mathscr{D}$ of independent variables in which Equation (2) is defined, then

$$\mathbb{u}(t) = \sum_{i=0}^{+\infty} a_i \exp(\lambda_i t)\mathbb{u}_i \tag{5}$$

Let us assume that the λ_i are ordered such that

$$\forall i \in \mathbb{N}_+^* \quad \forall j \in \mathbb{N}_+^*, \quad \{i \geqslant j\} \Rightarrow \{\Re(\lambda_i) \geqslant \Re(\lambda_j)\} \tag{6}$$

$$\forall i \in \mathbb{N}_+^* \quad \forall j \in \mathbb{N}_+^*, \quad \{i \geqslant j, \quad \Re(\lambda_i) = \Re(\lambda_j)\} \Rightarrow \{\Im(\lambda_i) \geqslant \Im(\lambda_j)\} \tag{7}$$

If λ_1 is real, after a long time, the disturbance is given by

$$\mathbb{u}(t) \underset{t \to +\infty}{\sim} a_1 \exp(\lambda_1 t)\mathbb{u}_1 \tag{8}$$

If λ_1 is complex ($\lambda_1 = \sigma_1 + \mathrm{i}\omega_1$, $\mathbb{u}_1 = \mathbb{u}_1^r + i\mathbb{u}_1^i$, $\lambda_2 = \underline{\lambda_1}$, $\mathbb{u}_2 = \underline{\mathbb{u}_1}$, $\underline{\lambda_1}$ and $\underline{\mathbb{u}_1}$ being the complex conjugates of λ_1 and $\mathbb{u}_1$, respectively), the disturbance $\mathbb{u}$ being real, a_1 is complex ($a_1 = a_1^r + ia_1^i$, $a_2 = \underline{a_1}$); after a long time, we have

$$\mathbb{u}(t) \underset{t \to +\infty}{\sim} 2 \exp(\sigma_1 t)[(a_1^r \mathbb{u}_1^r - a_1^i \mathbb{u}_1^i)\cos(\omega_1 t) - (a_1^r \mathbb{u}_1^i + a_1^i \mathbb{u}_1^r)\sin(\omega_1 t)] \tag{9}$$

Hence, comparing the asymptotic time behaviour of two disturbances, $\mathbb{u}^{(1)}$ and $\mathbb{u}^{(2)}$, of the same steady-state $\mathbb{U}_0$, results in the comparison of the moduli $|a_1^{(1)}|$ and $|a_1^{(2)}|$. If

$$|a_1^{(1)}| > |a_1^{(2)}|, \quad \text{then, after a long time, } \mathbb{u}^{(1)} \text{ is greater than } \mathbb{u}^{(2)} \tag{10}$$

Accordingly, the asymptotic solutions of the linearized equations give a way to classify the disturbances.

2.2. The adjoint approach

In order to find the spatial sensitivity to disturbances, we are using the adjoint equations, relative to the inner product $(f|g) = \int f\underline{g}$, $\underline{g}$ being the complex conjugate of g. The adjoint operator and associated boundary conditions $(\tilde{\mathscr{L}}, \tilde{\mathscr{B}})$ are defined such that if $\mathbb{u}$ satisfies $\mathscr{B}$ and $\tilde{\mathbb{u}}$ satisfies $\tilde{\mathscr{B}}$, then [22]

$$(\mathscr{L}(\mathbb{U}_0, \mathbb{u}), \tilde{\mathbb{u}}) = (\mathbb{u}, \tilde{\mathscr{L}}(\mathbb{U}_0, \tilde{\mathbb{u}})) \tag{11}$$

$\mathscr{L}(\mathbb{U}_0)$ and $\tilde{\mathscr{L}}(\mathbb{U}_0)$ have the same set of eigenvalues and the eigenvectors sets of the two operators $(\mathbb{u}_i)$ and $(\tilde{\mathbb{u}}_j)$, respectively, are bi-orthogonal:

$$(\mathbb{u}_i|\tilde{\mathbb{u}}_j) = \delta_{i,j} \tag{12}$$

Let $\mathbb{u}(t=0) \equiv \delta\mathbb{u} = \sum_{i=0}^{+\infty} a_i \mathbb{u}_i$ be a linear disturbance at time $t=0$ of the steady-state $\mathbb{U}_0$ characterized, for instance, by the velocity field $\mathbf{V}_0(\mathbf{U}_0, \mathbf{W}_0)$ and the temperature field Θ_0. The inner product on the perturbation is

$$(\mathbb{u}|\tilde{\mathbb{u}}) = \int_{\mathscr{D}} (u\underline{\tilde{u}} + w\underline{\tilde{w}} + \theta\underline{\tilde{\theta}})|J(\mathbf{x})|\,\mathrm{d}\Omega \tag{13}$$

The a_1 coefficient is then given by

$$a_1 = (\delta\mathbb{u}|\tilde{\mathbb{u}}_1) \tag{14}$$

For an impulse disturbance of a scalar field, such as the temperature, at location $\mathbf{x}_p$,

$$\delta\mathbb{T}(\mathbf{x}_p) = \begin{pmatrix} \mathbf{v} = 0 \\ \theta = \varepsilon\delta(\mathbf{x} - \mathbf{x}_p) \end{pmatrix}_{\forall \mathbf{x} \in \mathscr{D}} \tag{15}$$

with $\delta(\mathbf{x})$ representing the Dirac function, it results from the scalar product that

$$\begin{aligned} a_1 &= (\delta\mathbb{T}(\mathbf{x}_p)|\tilde{\mathbb{u}}_1) \\ &= \int_{\mathscr{D}} \varepsilon\delta(\mathbf{x} - \mathbf{x}_p)\underline{\tilde{\theta}}_1|J(\mathbf{x})|\,\mathrm{d}\Omega \\ &= \varepsilon\underline{\tilde{\theta}}_1(\mathbf{x}_p)|J(\mathbf{x}_p)| \end{aligned} \tag{16}$$

where $|J(\mathbf{x})|$ is the Jacobian. The response amplitude to a disturbance is then directly linked to the adjoint field.

In order to calculate the adjoint of the dominant eigenmode, two ways can be followed: the discrete adjoint approach and the continuous adjoint approach. In the first method, one works with the algebraic system that comes from the discretization of the fluid equations. The nonlinear PDEs are discretized, linearized (or linearized, discretized) and transposed. In the continuous approach [2], the adjoint system is obtained by integrating by parts the linearized flow equations; it is then discretized. The advantages and disadvantages of the two approaches were widely developed by Giles and Pierce [23]. Of course, in the limit of an infinite grid resolution, the two approaches should converge to the correct solution. The continuous approach is simpler to program and requires less memory unless pre-computation and storage of the linearized matrix can be avoided [17]. This last procedure seems very difficult to be applied in the case of our spectral collocation code. The continuous approach is then chosen in this work.

3. PHYSICAL AND MATHEMATICAL MODEL

The physical problem under consideration is the hydrodynamics of flows occurring in a floating zone-crystal growth device in a zero-gravity environment. This technique consists in translating

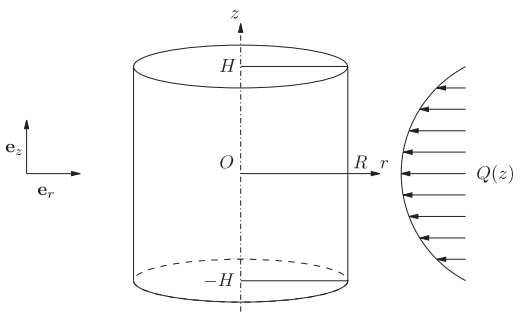

Figure 1. Geometry and coordinates system.

a feed rod through a heating coil; the material progressively melts and solidifies on a seed as a single crystal [24].

A simplified model of the liquid bridge is adopted. The Newtonian liquid is maintained by capillarity between two solid and isothermal planes at the uniform temperature T_m. The free surface is taken to be straight and non-deformable. The hypothesis of invariance by rotation leads to the axisymmetric configuration presented in Figure 1, where $\mathbf{e}_r$ and $\mathbf{e}_z$ are the radial and axial unit vectors, respectively, r and z being the corresponding coordinates. The origin O is located at the centre of the full liquid bridge. Then here, the domain $\mathscr{D}$ is defined by $(r,z) \in [0,R] \times [-H,H]$. The free surface is submitted to a steady heating flux $Q = Q_0\, q(z)$, with Q_0 the maximum heat flux density. The non-dimensional flux $q(z)$ is symmetric about the mid-plane defined by $z = 0$.

The capillary convective flows are governed by the Navier–Stokes and energy equations of which the Boussinesq non-dimensional expressions are

$$\begin{aligned} \frac{\partial \mathbf{V}}{\partial t} + (\mathbf{V}\cdot\boldsymbol{\nabla})\mathbf{V} &= -\boldsymbol{\nabla}P + Pr\left(\boldsymbol{\nabla}^2 - \frac{\mathbf{e}_r}{r^2}\right)\mathbf{V} \\ \frac{\partial \Theta}{\partial t} + \mathbf{V}\cdot\boldsymbol{\nabla}\Theta &= \boldsymbol{\nabla}^2\Theta \\ \boldsymbol{\nabla}\cdot\mathbf{V} &= 0 \end{aligned} \tag{17}$$

The operators are defined as follows: $\boldsymbol{\nabla} = \mathbf{e}_r\ (\partial/\partial r) + \mathbf{e}_z\ (\partial/\partial z)$ and $\boldsymbol{\nabla}^2 = (1/r)(\partial/\partial r)[(r(\partial/\partial r))] + \partial^2/\partial z^2$. Writing $\mathbf{V} = U\mathbf{e}_r + W\mathbf{e}_z$, one has also $\boldsymbol{\nabla}\cdot\mathbf{V} = (1/r)[\partial(rU)/\partial r] + (\partial W/\partial z)$ and $\mathbf{V}\cdot\boldsymbol{\nabla} = U(\partial/\partial r) + W(\partial/\partial z)$. The length, velocity, pressure and time scales, respectively, are R, κ/R, $\rho\,\kappa^2/R^2$ and R^2/κ, where ρ and κ are the density and the thermal diffusivity of the fluid, respectively. The temperature difference magnitude, ΔT, is defined from the imposed heat flux and the thermal conductivity, λ, $\Delta T = Q_0\, R/\lambda$. Then, the reduced temperature is $\Theta = (T - T_m)/\Delta T$, where T_m is the melting temperature. Non-dimensional parameters are introduced: the Marangoni ($Ma = -(\partial\sigma/\partial T)|_{T_m} R\Delta T/\mu\kappa$) and Prandtl ($Pr = \nu/\kappa$) numbers, where σ and μ, ν, respectively, stand for the surface tension and dynamic, kinematic viscosity. The Marangoni number is the ratio of the thermocapillary to thermal diffusion characteristic velocities. The Prandtl number is the ratio of the thermal to momentum characteristic diffusion times. The aspect ratio $A = H/R$ is here fixed to 1. To complete the equations set (17),

boundary conditions are specified:

$$
\begin{aligned}
z = \pm 1 \quad & \begin{cases} \mathbf{V} = \mathbf{0} & \text{(no-slip conditions)} \\ \Theta = 0 & \text{(imposed temperature)} \end{cases} \\
r = 1 \quad & \begin{cases} U = 0 & \text{(non-deformable free surface)} \\ \dfrac{\partial W}{\partial r} = -Ma \dfrac{\partial \Theta}{\partial z} f_n(z) & \text{(stress condition)} \\ \dfrac{\partial \Theta}{\partial r} = q(z) & \text{(heat flux)} \end{cases} \\
r = 0 \quad & \begin{cases} U = 0 \\ \dfrac{\partial W}{\partial r} = 0 & \text{(axial symmetry conditions)} \\ \dfrac{\partial \Theta}{\partial r} = 0 \end{cases}
\end{aligned}
\tag{18}
$$

Particular care must be taken to preserve the regularity of the model at the scale of the continuous medium by writing appropriate flux boundary conditions. For a complete discussion of this problem, we refer the reader to References [19, 25]. Indeed, at both extremities, where the free surface is in contact with the isothermal fusion/solidification fronts, the supplied heat flux must cancel. We have thus chosen $q(z) = (1 - z^2)^2$ to model the lateral heating device. In order to fulfil the no-slip condition on the solid boundaries, the flux of the momentum vertical component imposed by capillarity must also cancel. A simple way to regularize the stress condition is to introduce a function such as $f_n(z) = (1 - z^{2n})^2$, n being a positive integer, here fixed to 13 according to the results of Chénier *et al.* [19, 25].

3.1. The linearized equations

After linearization around the steady-state $\mathbb{U}_0 = (\mathbf{V}_0, \Theta_0)$, the equations for a perturbation $\mathbb{u} = (\mathbf{v}, \theta)$ are

$$
\left. \frac{\partial \mathbb{u}}{\partial t} \right|_{\mathbb{U}_0} = \mathscr{L}(\mathbb{U}_0, \mathbb{u}) \tag{19}
$$

within $\mathscr{D}$:

$$
\begin{aligned}
\frac{\partial u}{\partial t} &= -(\mathbf{v} \cdot \boldsymbol{\nabla}) U_0 - (\mathbf{V}_0 \cdot \boldsymbol{\nabla}) u - \frac{\partial p}{\partial r} + Pr \left(\Delta u - \frac{u}{r^2} \right) \\
\frac{\partial w}{\partial t} &= -(\mathbf{v} \cdot \boldsymbol{\nabla}) W_0 - (\mathbf{V}_0 \cdot \boldsymbol{\nabla}) w - \frac{\partial p}{\partial z} + Pr \Delta w \\
\frac{\partial \theta}{\partial t} &= -(\mathbf{v} \cdot \boldsymbol{\nabla}) \Theta_0 - (\mathbf{V}_0 \cdot \boldsymbol{\nabla}) \theta + \Delta \theta \\
\boldsymbol{\nabla} \cdot \mathbf{v} &= 0
\end{aligned}
\tag{20}
$$

and on the boundaries $\partial\mathscr{D}$:

$$
\begin{aligned}
z = \pm 1 \quad & \begin{cases} \mathbf{v} = \mathbf{0} \\ \theta = 0 \end{cases} \\
r = 1 \quad & \begin{cases} u = 0 \\ \dfrac{\partial w}{\partial r} = -Ma\,\dfrac{\partial \theta}{\partial z}\, f_n(z) \\ \dfrac{\partial \theta}{\partial r} = 0 \end{cases} \\
r = 0 \quad & \begin{cases} u = 0 \\ \dfrac{\partial w}{\partial r} = 0 \\ \dfrac{\partial \theta}{\partial r} = 0 \end{cases}
\end{aligned}
\tag{21}
$$

3.2. The adjoint system

In order to calculate the adjoint operator $\tilde{\mathscr{L}}(\mathbb{U}_0)$ as defined in Equation (11), we develop the Hermitian inner product in cylindrical coordinates:

$$
\begin{aligned}
(\mathscr{L}(\mathbb{U}_0, \mathbb{u})|\tilde{\mathbb{u}}) = \iint_{\mathscr{D}} \Bigg[& \left(-(\mathbf{v}\cdot\boldsymbol{\nabla})U_0 - (\mathbf{V}_0\cdot\boldsymbol{\nabla})u - \frac{\partial p}{\partial r} + Pr\left(\Delta u - \frac{u}{r^2}\right)\right)\underline{\tilde{u}} \\
& + \left(-(\mathbf{v}\cdot\boldsymbol{\nabla})W_0 - (\mathbf{V}_0\cdot\boldsymbol{\nabla})w - \frac{\partial p}{\partial z} + Pr\Delta w \right)\underline{\tilde{w}} \\
& + (-(\mathbf{v}\cdot\boldsymbol{\nabla})\Theta_0 - (\mathbf{V}_0\cdot\boldsymbol{\nabla})\theta + \Delta\theta)\underline{\tilde{\theta}} \\
& - (\boldsymbol{\nabla}\cdot\mathbf{v})\underline{\tilde{p}} \Bigg] r\,\mathrm{d}r\,\mathrm{d}z
\end{aligned}
\tag{22}
$$

Integration by parts leads to

$$
\begin{aligned}
(\mathscr{L}(\mathbb{U}_0, \mathbb{u})|\tilde{\mathbb{u}}) = \iint_{\mathscr{D}} \Bigg[& \left((\mathbf{V}_0\cdot\boldsymbol{\nabla})\underline{\tilde{u}} - \underline{\tilde{u}}\frac{\partial U_0}{\partial r} - \underline{\tilde{w}}\frac{\partial W_0}{\partial r} - \underline{\tilde{\theta}}\frac{\partial \Theta_0}{\partial r} + \frac{\partial \underline{\tilde{p}}}{\partial r} + Pr\left(\Delta\underline{\tilde{u}} - \frac{\underline{\tilde{u}}}{r^2}\right)\right) u \\
& + \left((\mathbf{V}_0\cdot\boldsymbol{\nabla})\underline{\tilde{w}} - \underline{\tilde{u}}\frac{\partial U_0}{\partial z} - \underline{\tilde{w}}\frac{\partial W_0}{\partial z} - \underline{\tilde{\theta}}\frac{\partial \Theta_0}{\partial z} + \frac{\partial \underline{\tilde{p}}}{\partial z} + Pr\Delta\underline{\tilde{w}} \right) w \\
& + ((\mathbf{V}_0\cdot\boldsymbol{\nabla})\underline{\tilde{\theta}} + \Delta\underline{\tilde{\theta}})\theta \\
& + (\boldsymbol{\nabla}\cdot\underline{\tilde{\mathbf{v}}})\,p \Bigg] r\,\mathrm{d}r\,\mathrm{d}z \\
& - \int_{\partial\mathscr{D}} \mathbf{J}\cdot\mathbf{n}\,\mathrm{d}\sigma
\end{aligned}
\tag{23}
$$

where $\mathbf{n}$ is the unit vector normal to the boundary $\partial\mathscr{D}$ of $\mathscr{D}$, directed outwards, and $\mathbf{J} = J_r\mathbf{e}_r + J_z\mathbf{e}_z$, with

$$\begin{aligned} J_r &= U_0(u\underline{\tilde{u}} + w\underline{\tilde{w}} + \theta\underline{\tilde{\theta}}) + u\underline{\tilde{p}} + \underline{\tilde{u}}p \\ &\quad + Pr\left(u\frac{\partial\underline{\tilde{u}}}{\partial r} - \underline{\tilde{u}}\frac{\partial u}{\partial r}\right) + Pr\left(w\frac{\partial\underline{\tilde{w}}}{\partial r} - \underline{\tilde{w}}\frac{\partial w}{\partial r}\right) + \theta\frac{\partial\underline{\tilde{\theta}}}{\partial r} - \underline{\tilde{\theta}}\frac{\partial\theta}{\partial r} \\ J_z &= W_0(u\underline{\tilde{u}} + w\underline{\tilde{w}} + \theta\underline{\tilde{\theta}}) + w\underline{\tilde{p}} + \underline{\tilde{w}}p \\ &\quad + Pr\left(u\frac{\partial\underline{\tilde{u}}}{\partial z} - \underline{\tilde{u}}\frac{\partial u}{\partial z}\right) + Pr\left(w\frac{\partial\underline{\tilde{w}}}{\partial z} - \underline{\tilde{w}}\frac{\partial w}{\partial z}\right) + \theta\frac{\partial\underline{\tilde{\theta}}}{\partial z} - \underline{\tilde{\theta}}\frac{\partial\theta}{\partial z} \end{aligned} \tag{24}$$

The boundary conditions of the adjoint system are given by $\int_{\partial\mathscr{D}} \mathbf{J}\cdot\mathbf{n}\,\mathrm{d}\sigma = 0$. Taking into account the boundary conditions (18) and (21), it then follows that

- At $r = 0$,

$$\int_{-1}^{1}\left[Pr\left(-\underline{\tilde{u}}\frac{\partial u}{\partial r} + w\frac{\partial\underline{\tilde{w}}}{\partial r}\right) + \theta\frac{\partial\underline{\tilde{\theta}}}{\partial r} + \underline{\tilde{u}}p\right]\mathrm{d}z = 0 \tag{25}$$

  This relation is satisfied if

$$\tilde{u} = 0, \quad \frac{\partial\tilde{w}}{\partial r} = 0, \quad \frac{\partial\tilde{\theta}}{\partial r} = 0 \tag{26}$$

- At $r = 1$,

$$\begin{aligned} &\int_{-1}^{1}\left[Pr\left(-\underline{\tilde{u}}\frac{\partial u}{\partial r} + w\frac{\partial\underline{\tilde{w}}}{\partial r} - \underline{\tilde{w}}\frac{\partial w}{\partial r}\right) + \theta\frac{\partial\underline{\tilde{\theta}}}{\partial r} + \underline{\tilde{u}}p\right]\mathrm{d}z \\ &= \int_{-1}^{1}\left[-Pr\underline{\tilde{u}}\frac{\partial u}{\partial r} + Prw\frac{\partial\underline{\tilde{w}}}{\partial r} + PrMaf_n(z)\underline{\tilde{w}}\frac{\partial\theta}{\partial z} + \theta\frac{\partial\underline{\tilde{\theta}}}{\partial r} + \underline{\tilde{u}}p\right]\mathrm{d}z \\ &= \underbrace{[\theta\underline{\tilde{w}}PrMaf_n(z)]}_{=0} + \int_{-1}^{1}\left[\left(p - Pr\frac{\partial u}{\partial r}\right)\underline{\tilde{u}} + Prw\frac{\partial\underline{\tilde{w}}}{\partial r} - PrMa\theta\frac{\partial\underline{\tilde{w}}\,f_n(z)}{\partial z} + \theta\frac{\partial\underline{\tilde{\theta}}}{\partial r}\right]\mathrm{d}z \\ &= \int_{-1}^{1}\left[\left(p - Pr\frac{\partial u}{\partial r}\right)\underline{\tilde{u}} + Prw\frac{\partial\underline{\tilde{w}}}{\partial r} + \theta\left(\frac{\partial\underline{\tilde{\theta}}}{\partial r} - PrMa\frac{\partial\underline{\tilde{w}}\,f_n}{\partial z}\right)\right]\mathrm{d}z \\ &= 0 \end{aligned} \tag{27}$$

  This relation is satisfied if

$$\tilde{u} = 0, \quad \frac{\partial\tilde{w}}{\partial r} = 0, \quad \frac{\partial\tilde{\theta}}{\partial r} = PrMa\frac{\partial\underline{\tilde{w}}\,f_n}{\partial z} \tag{28}$$

- At last, from the relation at $z = \pm 1$,

$$\int_0^1 \left[-Pr \left(\underline{\tilde{u}} \frac{\partial u}{\partial z} + \underline{\tilde{w}} \frac{\partial w}{\partial z} \right) - \underline{\tilde{\theta}} \frac{\partial \theta}{\partial z} + \underline{\tilde{w}} p \right] \mathrm{d}r = 0 \tag{29}$$

it can be deduced that, on these boundaries

$$\tilde{u} = 0, \quad \tilde{w} = 0, \quad \tilde{\theta} = 0 \tag{30}$$

The relation deduced from Equations (2) and (11),

$$\left(\frac{\partial \mathbb{u}}{\partial t}, \tilde{\mathbb{u}} \right) = - \left(\mathbb{u}, \frac{\partial \tilde{\mathbb{u}}}{\partial t} \right) + \frac{\partial}{\partial t} (\mathbb{u}, \tilde{\mathbb{u}}) \tag{31}$$

leads to the adjoint equation,

$$- \frac{\partial \tilde{\mathbb{u}}}{\partial t} = \tilde{\mathscr{L}} (\mathbb{U}_0, \tilde{\mathbb{u}}) \tag{32}$$

so that

$$\frac{\partial}{\partial t} (\mathbb{u}, \tilde{\mathbb{u}}) = 0 \tag{33}$$

Note the sign change of the time which produces a reversal of causality in time-varying problems so that the adjoint parabolic operator is well posed only if one integrates backwards in time with initial conditions obtained at final time from the direct system. This backward approach was used by Luchini and Bottaro [14, 15] in case of Görtler vortices and Stokes's first problem.

Let

$$\tilde{\mathbb{u}}(t) = \sum_{i=0}^{+\infty} \tilde{a}_i \exp(-\tilde{\lambda}_i t) \tilde{\mathbb{u}} \tag{34}$$

be a solution of Equation (32). Substituting Equations (5) and (34) in Equation (33), the bi-orthogonality relation (12) insures the well-known relation $\tilde{\lambda}_i = \underline{\lambda}_i$.

In summary, the adjoint system is

$$\begin{gathered}
\frac{\partial \tilde{u}}{\partial t} + (\mathbf{V}_0 \cdot \boldsymbol{\nabla}) \tilde{u} - \tilde{u} \frac{\partial U_0}{\partial r} - \tilde{w} \frac{\partial W_0}{\partial r} - \tilde{\theta} \frac{\partial \Theta_0}{\partial r} = - \frac{\partial \tilde{p}}{\partial r} - Pr \left(\Delta \tilde{u} - \frac{\tilde{u}}{r^2} \right) \\
\frac{\partial \tilde{w}}{\partial t} + (\mathbf{V}_0 \cdot \boldsymbol{\nabla}) \tilde{w} - \tilde{u} \frac{\partial U_0}{\partial z} - \tilde{w} \frac{\partial W_0}{\partial z} - \tilde{\theta} \frac{\partial \Theta_0}{\partial z} = - \frac{\partial \tilde{p}}{\partial z} - Pr \Delta \tilde{w} \\
\frac{\partial \tilde{\theta}}{\partial t} + (\mathbf{V}_0 \cdot \boldsymbol{\nabla}) \tilde{\theta} = - \Delta \tilde{\theta} \\
\boldsymbol{\nabla} \cdot \tilde{\mathbf{v}} = 0
\end{gathered} \tag{35}$$

with the following boundary conditions:

$$
\begin{aligned}
z = \pm 1 \quad & \begin{cases} \tilde{\mathbf{v}} = \mathbf{0} \\ \tilde{\theta} = 0 \end{cases} \\
r = 0 \quad & \begin{cases} \tilde{u} = 0 \\ \dfrac{\partial \tilde{w}}{\partial r} = 0 \\ \dfrac{\partial \tilde{\theta}}{\partial r} = 0 \end{cases} \\
r = 1 \quad & \begin{cases} \tilde{u} = 0 \\ \dfrac{\partial \tilde{w}}{\partial r} = 0 \\ \dfrac{\partial \tilde{\theta}}{\partial r} = Pr\, Ma \dfrac{\partial \tilde{w}\, f_n}{\partial z} \end{cases}
\end{aligned}
\tag{36}
$$

4. NUMERICAL DETERMINATION OF THE RESPONSE AMPLITUDE

4.1. The numerical tools

In order to calculate the response amplitude, a_1, through relations (8) or (9) and (14), complementary numerical tools, described in detail in References [18, 19], are used. In systems (20), (21) and (35), (36), the evaluation of the space derivatives is based on a pseudospectral Chebyshev collocation method [26] with radial Gauss–Radau and axial Gauss–Lobatto grids $N_r \times N_z$, fixed to 70×100 in this study in agreement with the results of References [18, 19]. A projection-diffusion algorithm is used to uncouple the velocity and pressure fields [27]. The resulting time ordinary differential system is solved by a usual second-order finite difference scheme with an implicit treatment of the diffusion terms. Stringent criteria, which are detailed in Reference [28], have been applied to assess the overall accuracy of the results. Correlated with a time-marching procedure (which supplies only stable steady or oscillatory flows), specific tools (based on a continuation process) have been implemented for drawing, in the parameters space, the loci of the steady states, stable or not. The leading eigenmodes of the linearized problem and of its adjoint system are computed using two codes based on the Arnoldi's method: one developed by ourselves and the other using the Arpack library [29]. In the case of the adjoint system, time must be reversed as mentioned above, preventing anti-dissipation effects when solving Equation (35), but the initial values are arbitrary here.

4.2. Stability map

The present results constitute a continuation of the study of Chénier *et al.* [19] in which the linear stability of the thermocapillary flow, at $Pr = 0.01$, has been widely investigated. In particular, due to the explicit introduction of a small length scale by the regularizing

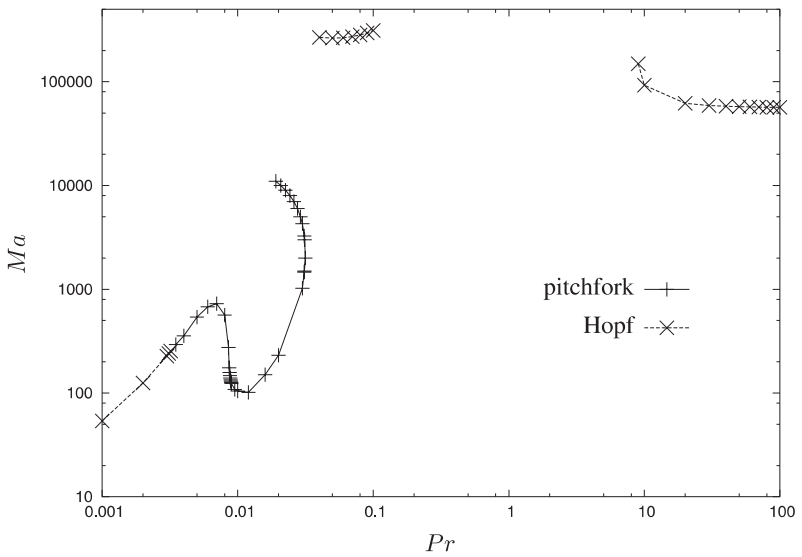

Figure 2. Stability map with respect to the *Ma* and *Pr* numbers values.

function f_n, a sub-critical pitchfork bifurcation followed by saddle-nodes bifurcations on the continuation curve was observed. The coexistence of multiple stable steady states, which are either reflection symmetric or not with respect to the mid-plane, was established. In this work, the symmetric steady state, the dominant characteristic values of the linearized system and the bifurcation threshold are followed with respect to the Prandtl number value leading to the stability map in Figure 2.

Starting from the smallest *Pr* values, the stability map falls into several regions:

- $Pr \in [10^{-3}, 3.4 \times 10^{-3}]$: Hopf bifurcations,
- $Pr \in [3.4 \times 10^{-3}, 3.15 \times 10^{-2}]$, $Ma \lesssim 10^3$: sub-critical pitchfork bifurcations,
- $Pr \in [1.9 \times 10^{-2}, 3.15 \times 10^{-2}]$, $Ma \gtrsim 10^3$: pitchfork bifurcations,
- $Pr \in [4 \times 10^{-2}, 10^{-1}]$: Hopf bifurcations,
- $Pr \in [9, 100]$: Hopf bifurcations.

Some leading eigenvalues in the vicinity of the transition are given in Table I.

Some comments can be pointed out.

- For $Pr = 3.0 \times 10^{-3}$, the real parts of the two first leading eigenvalues are close together (see Table I) and cross at a co-dimension 2 point, explaining the change of bifurcation type.
- For $Pr \in [1.9 \times 10^{-2}, 3.15 \times 10^{-2}]$, reflection-symmetric stable steady states exist at low and high Marangoni values. The schematic bifurcation diagram with respect to the Marangoni number value, which was highlighted in Reference [19] at $Pr = 0.01$, can now be completed, for the here concerned *Pr* values, as shown in Figure 3. The stable symmetric steady state loses its stability via a sub-critical pitchfork bifurcation and becomes stable again via another pitchfork bifurcation at a higher Marangoni value. On the two branches

Table I. Leading eigenvalues of $\mathscr{L}$ and $\tilde{\mathscr{L}}$ and their relative difference δ.

Prandtl	Marangoni	Direct $\lambda_d = \sigma_d + \mathrm{i}\omega_d$		Adjoint $\lambda_a = \sigma_a + \mathrm{i}\omega_a$		δ
		σ_d	ω_d	σ_a	ω_a	
1.000×10^{2}	5.660×10^{4}	-1.2190×10^{-2}	1.2453×10^{2}	-1.2295×10^{-2}	1.2453×10^{2}	$8 \times 10^{-5}\%$
1.000×10^{1}	9.260×10^{4}	2.7881×10^{-3}	1.0866×10^{2}	2.8134×10^{-3}	1.0866×10^{2}	$2 \times 10^{-5}\%$
3.100×10^{-2}	1.500×10^{3}	8.4271×10^{-4}	0.0000	8.3692×10^{-4}	0.0000	0.6%
1.000×10^{-2}	1.060×10^{2}	1.7000×10^{-4}	0.0000	1.7050×10^{-4}	0.0000	0.3%
3.000×10^{-3}	2.250×10^{2}	-7.1228×10^{-3}	0.0000	-6.6489×10^{-3}	0.0000	6%
3.000×10^{-3}	2.250×10^{2}	-2.1170×10^{-2}	1.2894×10^{1}	-2.2512×10^{-2}	1.2893×10^{1}	0.01%
2.000×10^{-3}	1.240×10^{2}	-1.3067×10^{-2}	8.6502	-1.4175×10^{-2}	8.6202	0.3%

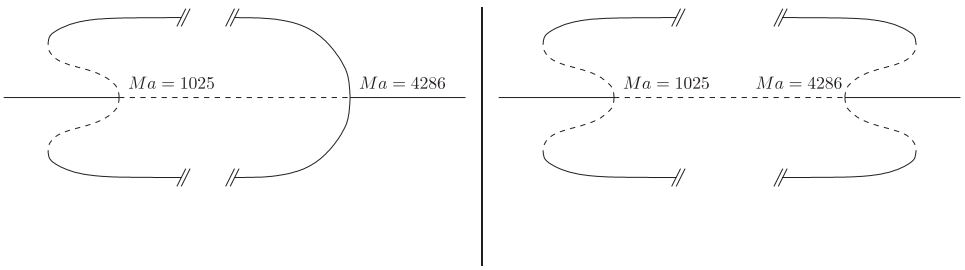

Figure 3. Two scenaries with respect to the increasing Marangoni number value, at $Pr = 0.03$. The solid curves indicate stable steady states while the dashed curves correspond to unstable steady states. On the left, the symmetric stable steady state becomes unstable via a sub-critical pitchfork bifurcation and finds its stability again through a super-critical pitchfork bifurcation. On the right, both pitchfork bifurcations are sub-critical. On the curves issued from the first pitchfork bifurcation, corresponding to asymmetric steady states, several saddle-nodes bifurcations occur [19].

of the continuation curve issued from the pitchfork bifurcation at low Marangoni value, saddle nodes are encountered giving rise to stable asymmetric steady states.

- Around $Pr = 1$, the flow unsteadiness has not been reached; this confirms Kasperski *et al.*'s results [30], obtained by solving the time-dependent non-linear system.
- The Hopf bifurcations thresholds at high Marangoni number values are independent of the Prandtl number value (except for $Pr \in [10^{-1}, 9]$), contrary to their linear behaviour with respect to low Prandtl number values.

We shall check our adjoint approach before applying it in order to determine the most sensitive loci to disturbances, for flows corresponding to the various regions of the bifurcation map.

4.3. Tools validation

The operators $\mathscr{L}(\mathbb{U}_0, \mathbb{u})$ and $\tilde{\mathscr{L}}(\mathbb{U}_0, \tilde{\mathbb{u}})$ must have the same set of eigenvalues; therefore, their leading eigenvalues have to be equal. Table I gives these values, obtained with the two Arnoldi procedures, for some pairs of Prandtl and Marangoni number values corresponding

to the bifurcations regions in the parameters map: the agreement is quite good as shown by their relative difference values $\delta = (|\lambda_d - \lambda_a|)/|\lambda_a|$.

The bi-orthogonality property was verified by calculating the inner product of the direct eigenbasis with the adjoint eigenbasis for the 11 first leading eigenvectors of each basis. The bi-orthogonality is satisfied to at least 10^{-4}. Of course, while using the discrete adjoint method, these properties are automatically verified, but this does not prove the eigenvectors' accuracy, which is linked to the discretization itself.

4.4. *Validation of the method*

We shall now compare the time-dependent and adjoint approaches on various disturbance types.

Given

$$\mathbb{u}(t) \underset{t\to+\infty}{\sim} a_1 \exp(\lambda_1 t)\mathbb{u}_1 \tag{37}$$

the absolute value of the ratio

$$\frac{\mathbb{u}_{i_{p2},j_{p2}}(T)}{\mathbb{u}_{i_{p1},j_{p1}}(T)} = \frac{a_1(i_{p2},j_{p2})}{a_1(i_{p1},j_{p1})} \tag{38}$$

makes possible the comparison of the response, at the same large time T, to initial disturbances at points (i_{p1},j_{p1}) and (i_{p2},j_{p2}), respectively.

The same ratio is calculated from the inner product:

$$\frac{a_1(i_{p2},j_{p2})}{a_1(i_{p1},j_{p1})} = \frac{(\delta\mathbb{u}(i_{p1},j_{p1})|\tilde{\mathbb{u}}_1)}{(\delta\mathbb{u}(i_{p2},j_{p2})|\tilde{\mathbb{u}}_1)} \tag{39}$$

4.4.1. Disturbance at a local position of the temperature field near a stationary bifurcation point. At the parameter values $Pr = 10^{-2}$ and $Ma = 104.4$, the steady 2D thermocapillary flow loses its stability through a sub-critical pitchfork bifurcation [19].

Figure 4 shows the iso-level lines of, respectively, the steady temperature field, the temperature component of the leading and corresponding adjoint eigenvectors, all normalized with respect to their maximum absolute value. The solid curves designate positive temperatures and the dash curves, negative temperatures.

In case of axisymmetric configuration, Equation (16) is written as

$$\begin{aligned} a_1 &= (\delta\mathbb{T}(r_p,z_p)|\tilde{\mathbb{u}}_1) \\ &= \int_{-1}^{1}\int_{0}^{1} \varepsilon\delta(r-r_p)\delta(z-z_p)\underline{\tilde{\theta}}_1 r\,\mathrm{d}r\,\mathrm{d}z \\ &= \varepsilon\underline{\tilde{\theta}}_1(r_p,z_p)r_p \end{aligned} \tag{40}$$

Figure 5, which presents the iso-level lines of $\underline{\tilde{\theta}}_1 r$, indicates that the most sensitive region to temperature disturbance of the Dirac type is situated on the free surface, near the horizontal

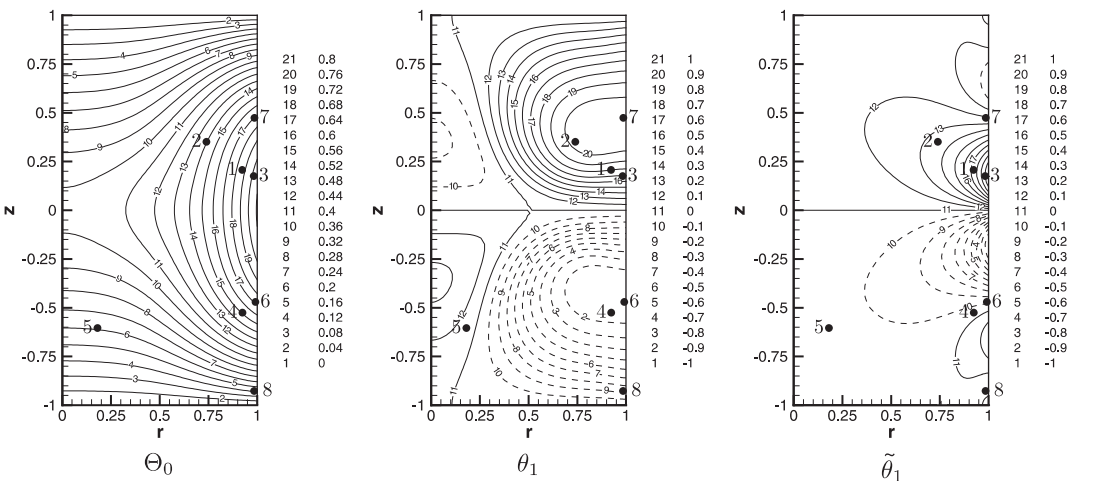

Figure 4. Steady temperature, temperature component of the leading and corresponding adjoint eigenvectors, both normalized with their maximum absolute value, at $Pr = 10^{-2}$ and $Ma = 106$. The numbered points correspond to the loci where the time and adjoint approaches are compared.

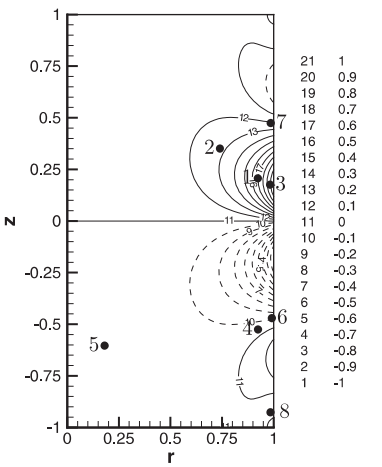

Figure 5. Map of the steady flow sensitivity to temperature disturbances of Dirac type at $Pr = 10^{-2}$ and $Ma = 106$. The numbered points correspond to the loci where the time and adjoint approaches are compared.

mid-plane. Note that it does not coincide with the maximum of the direct leading eigenvector. Regarding the computer cost, the calculation of $\tilde{\mathfrak{v}}_1$ with Arpack approximately requires 10^5 calls to the solver of the time-dependent linearized system (35)–(36).

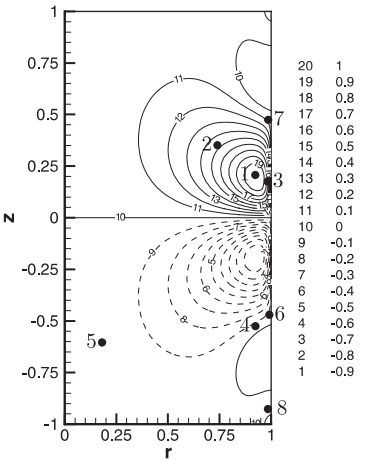

Figure 6. Numerical sensitivity map of the steady flow at $Pr = 10^{-2}$ and $Ma = 106$. The numbered points correspond to the loci where the time and adjoint approaches are compared.

The analytic Dirac distribution is replaced, in the numerical tools, by the Kronecker symbol. The numerical perturbation, at $t = 0$, $\delta\mathbb{T}(i_p, j_p)$, at a collocation point, (i_p, j_p), then, is

$$\delta\mathbb{T}(i_p, j_p) = \begin{pmatrix} u_{i,j} = 0 \\ w_{i,j} = 0 \\ \theta_{i,j} = \delta_{i,i_p}\delta_{j,j_p} \end{pmatrix}_{\forall (i,j) \in [0, N_r - 1] \times [0, N_z - 1]} \tag{41}$$

On the one hand, the coefficient $a_1^{\text{temp},k}$, for each disturbance $k = 1, \ldots, 8$, as indicated in Figures 4–6, has been measured by solving the time-dependent linearized system Equation (19) on a non-dimensional time $T = 450$ (with a time step equal to 10^{-3}). On the other hand, the coefficient $a_1^{\text{adj},k}$ has been calculated by the integral relation

$$\begin{aligned} a_1^{\text{adj}} &= (\delta\mathbb{T}(i_p, j_p) | \tilde{\mathbb{u}}_1) \\ &= \oint\!\!\oint_{\mathscr{D}} \delta_{i,i_p}\delta_{i,j_p}\tilde{\underline{\theta}}_1 r_i \, \mathrm{d}r_i \, \mathrm{d}z_j \\ &= r(i_p)\tilde{\underline{\theta}}_1(i_p, j_p) \oint\!\!\oint_{\mathscr{D}} \delta_{i,i_p}\delta_{i,j_p} \, \mathrm{d}r_i \, \mathrm{d}z_j \end{aligned} \tag{42}$$

where $\oint\!\!\oint_{\mathscr{D}}$ is the numerical integral value on a collocation non-uniform grid.

In Table II the amplitude coefficient values $a_1^{\text{temp},k}$ and $a_1^{\text{adj},k}$, respectively, normalized with respect to their maximum absolute value, are arranged in descending order. The two approaches are in good agreement.

Table II. Response coefficients to temperature perturbations of Dirac type, a_1^{temp} and a_1^{adj}, normalized with their respective maximum absolute value, in descending order.

Disturbance k	$a_1^{\text{temp},k}/\max_l a_1^{\text{temp},l}$	$a_1^{\text{adj},k}/\max_l a_1^{\text{adj},l}$
1	1.0000	1.0000
2	5.0683×10^{-1}	5.0124×10^{-1}
3	1.9290×10^{-1}	1.3916×10^{-1}
7	1.3366×10^{-2}	1.4164×10^{-2}
8	-5.4637×10^{-3}	-6.8331×10^{-3}
6	-1.3366×10^{-2}	-1.4164×10^{-2}
5	-2.6707×10^{-2}	-2.5543×10^{-2}
4	-4.2433×10^{-2}	-5.3174×10^{-2}

The a_1^{adj} coefficient was then calculated by the scalar product (42), for each element of the disturbances set (41). The corresponding iso-level lines are shown in Figure 6 giving the numerical sensitivity map.

The maps, Figures 5 and 6, are not the same because of the difference between the integral of Dirac and Kronecker distributions. If the disturbances set (41) is replaced by

$$\delta\mathbb{T}(i_p, j_p) = \left(\begin{array}{l} u_{i,j} = 0 \\ w_{i,j} = 0 \\ \theta_{i,j} = \dfrac{\delta_{i,i_p}\delta_{j,j_p}}{\oint\!\!\oint_{\mathscr{D}} \delta_{i,i_p}\delta_{i,j_p}\,\mathrm{d}r_i\,\mathrm{d}z_j} \end{array} \right)_{\forall (i,j)\in[0,N_r-1]\times[0,N_z-1]} \tag{43}$$

the two maps will be the same.

It might be emphasized that the computation costs of, on the one hand, the leading adjoint eigenmode and, by the way, the sensitivity map and, on the other hand, the time evolution of only one perturbation are of the same order.

4.4.2. Disturbance at a local position of the temperature field near a Hopf bifurcation point. For the parameters values $Pr = 2 \times 10^{-3}$ and $Ma = 124.8$, two complex conjugate eigenvalues cross the imaginary axis and the steady flow becomes periodic via a Hopf bifurcation. The tests have been performed at $Ma = 130$, where $(\lambda_1 = \sigma_1 + \mathrm{i}\omega_1 = 4.98 \times 10^{-2} + \mathrm{i}8.85)$.

Figure 7 shows the iso-level lines of the steady temperature field and the temperature component moduli of the leading and corresponding adjoint eigenvectors; the moduli have been normalized by their maximum value.

Following Equation (16), the most sensitive zone to temperature disturbance is situated on the free surface at $z = 0.25$.

In order to obtain $|a_1^{\text{temp},k}|$ for each k perturbation (labelled from 1 to 6 in Figure 7), we used the linearized time-dependent code to calculate the flow field during a non-dimensional time equal to 60 (time step equal to 2×10^{-4}).

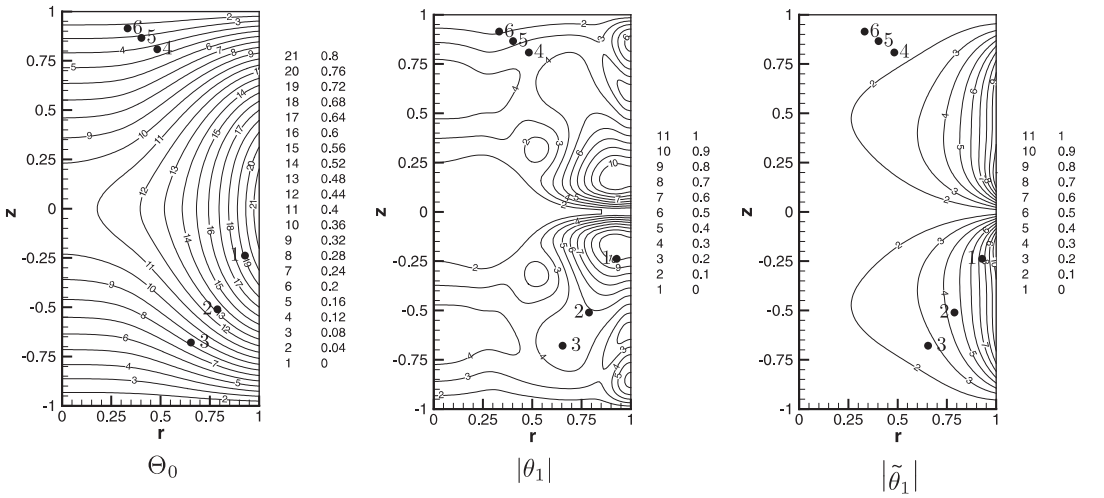

Figure 7. Iso-level lines of the steady temperature field and the temperature component moduli of the leading and corresponding adjoint eigenvectors at $Pr = 2 \times 10^{-3}$ and $Ma = 130$; the moduli are normalized by their maximum value. The numbered points correspond to the loci where the time and adjoint approaches are compared.

Table III. Response coefficients, a_1, in descending order, to disturbances near a Hopf bifurcation, normalized with their maximum modulus.

Disturbance k	$\lvert a_1^{\text{temp},k}\rvert / \max_l \lvert a_1^{\text{temp},l}\rvert$	$\lvert a_1^{\text{adj},k}\rvert / \max_l \lvert a_1^{\text{adj},l}\rvert$
1	1.0000	1.0000
2	6.2500×10^{-1}	5.3699×10^{-1}
3	2.4837×10^{-1}	2.5673×10^{-1}
4	7.3052×10^{-2}	1.1383×10^{-1}
5	3.0844×10^{-2}	7.1312×10^{-2}
6	1.2256×10^{-2}	4.1375×10^{-2}

This perturbation behaviour, in the vicinity of the bifurcation point, agrees with relation (9), i.e.

$$\mathbb{u}(t) \underset{t \to +\infty}{\sim} 2 \exp(\sigma_1 t)[(a_1^r \mathbb{u}_1^r - a_1^i \mathbb{u}_1^i)\cos(\omega_1 t) - (a_1^r \mathbb{u}_1^i + a_1^i \mathbb{u}_1^r)\sin(\omega_1 t)] \tag{44}$$

$|a_1^{\text{temp},k}|$ was then estimated from a fit of the exponential envelope of one component of the flow field for a perturbation done at each labelled k point of the grid.

The coefficient $a_1^{\text{adj},k}$ was calculated in the same way as in the case of a stationary bifurcation. Table III shows a comparison of the two approaches, showing their good agreement.

4.4.3. Velocity disturbance. Given an initial velocity disturbance $\delta\mathbb{u}$,

$$\delta\mathbb{u} = \begin{pmatrix} u_{r,z} = \delta u \\ w_{r,z} = \delta w \\ \theta_{r,z} = 0 \end{pmatrix}_{\forall (r,z)\in\mathscr{D}} \tag{45}$$

a_1 is then equal to

$$\begin{aligned} a_1 &= (\delta\mathbb{u}|\tilde{\mathbb{u}}_1) \\ &= \int_{-1}^{1}\int_{0}^{1} (\delta u\underline{\tilde{u}}_1 + \delta w\underline{\tilde{w}}_1) r\,\mathrm{d}r\,\mathrm{d}z \end{aligned} \tag{46}$$

With the relations between the velocity components $\tilde{u}_1$ and $\tilde{w}_1$ and the stream function $\tilde{\psi}_1$

$$\tilde{u}_1 = \frac{\partial\tilde{\psi}_1}{\partial z}, \quad \tilde{w}_1 = -\frac{1}{r}\frac{\partial r\tilde{\psi}_1}{\partial r} \tag{47}$$

where the adjoint velocity vectors are tangent to the $r\tilde{\psi}_1$ iso-lines.

Equation (46) becomes

$$\begin{aligned} a_1 &= \int_{-1}^{1}\int_{0}^{1} (\delta u\underline{\tilde{u}}_1 + \delta w\underline{\tilde{w}}_1) r\,\mathrm{d}r\,\mathrm{d}z \\ &= \int_{-1}^{1}\int_{0}^{1} \left(\delta u\frac{\partial\underline{\tilde{\psi}}_1}{\partial z} + \delta w\left(-\frac{1}{r}\frac{\partial r\underline{\tilde{\psi}}_1}{\partial r}\right)\right) r\,\mathrm{d}r\,\mathrm{d}z \\ &= \int_{r=0}^{r=1} \left(\underbrace{[r\delta u\underline{\tilde{\psi}}_1]_{z=-1}^{z=1}}_{=0} - \int_{-1}^{1}\underline{\tilde{\psi}}_1\frac{\partial r\delta u}{\partial z}\,\mathrm{d}z\right)\mathrm{d}r - \int_{z=-1}^{z=1}\left(\underbrace{[r\delta w\underline{\tilde{\psi}}_1]_{r=0}^{r=1}}_{=0} - \int_{r=0}^{r=1} r\underline{\tilde{\psi}}_1\frac{\partial\delta w}{\partial r}\,\mathrm{d}r\right)\mathrm{d}z \\ &= \int_{-1}^{1}\int_{0}^{1}\left(-\frac{\partial\delta u}{\partial z} + \frac{\partial\delta w}{\partial r}\right)\underline{\tilde{\psi}}_1 r\,\mathrm{d}r\,\mathrm{d}z \\ &= -\int_{-1}^{1}\int_{0}^{1}\delta\omega\underline{\tilde{\psi}}_1 r\,\mathrm{d}r\,\mathrm{d}z \end{aligned} \tag{48}$$

where $\delta\omega$ is the vorticity of the perturbation. Therefore, velocity and vorticity sources in the flow are, respectively, weighted by the adjoint velocity field and the adjoint stream function.

The steady state at $Pr = 10^{-2}$ and $Ma = 106$ has been disturbed by a solenoidal velocity field since it is expanded on divergence-free eigenvectors. The perturbation is defined as

$$\delta\mathbb{U}_g(r_p, z_p) = \begin{pmatrix} \boldsymbol{\nabla}\times\mathbf{A}(r_p, z_p) \\ 0 \end{pmatrix} \tag{49}$$

with

$$\mathbf{A} = (0, A_\varphi, 0) \tag{50}$$

Table IV. Response coefficients, a_1^{temp} and a_1^{adj}, normalized with their maximum absolute value, in descending order in case of Gaussian velocity perturbations.

Perturbation k	$a_1^{\text{temp},k}/\max_l a_1^{\text{temp},l}$	$a_1^{\text{adj},k}/\max_l a_1^{\text{adj},l}$
1	2.0907×10^{-1}	2.0884×10^{-1}
2	-1.4891×10^{-1}	-1.4882×10^{-1}
3	-5.4658×10^{-2}	-5.5459×10^{-2}
4	-2.2329×10^{-2}	-2.2314×10^{-2}
5	-1.7178×10^{-2}	-1.7200×10^{-2}
6	-1.0000	-1.0000
7	-3.7769×10^{-1}	-3.7749×10^{-1}
8	-1.0000	-1.0000

A_φ has been chosen as the following Gaussian function centred on the collocation point (r_p, z_p) and cancelling on the boundaries

$$A_\varphi(r_p, z_p) = \frac{1}{\beta} r^2(1-r)^2(z^2-1)^2 \mathrm{e}^{\alpha((r-r_p)^2+(z-z_p)^2)} \tag{51}$$

so that the velocity perturbation field is

$$\delta\mathbb{U}_g(r_p, z_p) = \begin{pmatrix} u_{r,z} \\ w_{r,z} \\ \theta_{r,z} \end{pmatrix}_{\forall (r,z)\in\mathscr{D}} \tag{52}$$

with

$$\begin{aligned} u_{r,z} &= -\frac{1}{\beta} 2r^2(1-r)^2(z^2-1)[2z + \alpha(z-z_p)(z^2-1)]\mathrm{e}^{\alpha((r-r_p)^2+(z-z_p)^2)} \\ w_{r,z} &= \frac{1}{\beta} r(1-r)(z^2-1)^2[3-5r+2\alpha r(r-r_p)(1-r)]\mathrm{e}^{\alpha((r-r_p)^2+(z-z_p)^2)} \\ \theta_{r,z} &= 0 \end{aligned} \tag{53}$$

where

$$\beta = \sqrt{(r_p^2(1-r_p)^2(z_p^2-1)z_p)^2 + (r_p(1-r_p)(z_p^2-1)^2(3-5r_p))^2} \tag{54}$$

and α is here equal to -10^{-2}. In Table IV the normalized response amplitudes, respectively, obtained with the time-dependent code and the inner product (13) are given.

Figure 8 presents $|a_1^{\text{adj},k}/\max_l a_1^{\text{adj},l}|$ iso-lines corresponding to disturbances at all collocation points; owing to the non uniformity of the grid, each perturbation was normalized by its associated kinetic energy. The most sensible point is situated near the symmetry axis.

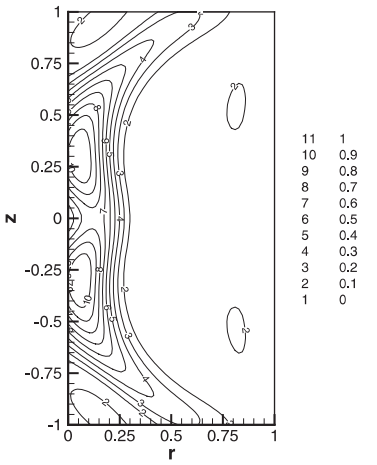

Figure 8. Sensitivity map of the steady state to the leading eigenmode at $Pr = 10^{-2}$ and $Ma = 106$, for the perturbations set $\delta\mathbb{U}_g(i_p, j_p)$, normalized with their associated kinetic energy.

5. APPLICATION TO THE STABILITY STUDY

One of the purposes of our method is to help the understanding of the instability mechanisms. We therefore, now, apply it to the four regions, distinguished above on the stability map of Figure 2, which correspond to transitions of the stable steady state to an unstable steady flow (sub-critical pitchfork bifurcation) or to a periodic steady flow (Hopf bifurcation).

Figures 9 and 10 depict components of the steady flows fields for four pairs of *Pr–Ma* values, related to the regions under consideration. The solid curves of the stream function designate counter-clockwise circulation and the dash curves, clockwise circulation. The solid contours of the vorticity field are related to positive vorticity, and the dash contours to negative vorticity. Figure 11 shows the maps of sensitivity, $\underline{\tilde{\psi}}_1 r$, to vorticity disturbances. The maps of sensitivity to perturbations of the Dirac type in temperature, $\underline{\tilde{\theta}}_1 r$, have also been calculated, but are not shown here. The crosses and circles in the figures indicate the points corresponding to the largest response to temperature and vorticity disturbances, respectively.

In case of temperature disturbances, the most sensitive point is always situated on the free surface. Distinction must be made between high and low Prandtl number values.

- At $Pr > 1$, the most sensitive location coincides with the maximum value of the steady-state temperature. The most sensitive region to vorticity disturbance is situated in the middle of the rotating cells, but nothing can be pointed out there neither in the fields components of the flow nor with the leading eigenvector, nor in the results of the energy analysis performed by Bouizi [28] as introduced by Wanschura *et al.* [31].
- At $Pr < 1$, the most sensitive location to perturbation in temperature is not very far from the temperature maximum of the steady flow. However, it seems linked to the vorticity tongue, which is advected from the solid boundaries and confined, near the mid-plane, between the main cell, of opposite vorticity sign, and the free surface; a Fjørtøft-like necessary criterion for instability [32] is here fulfilled.

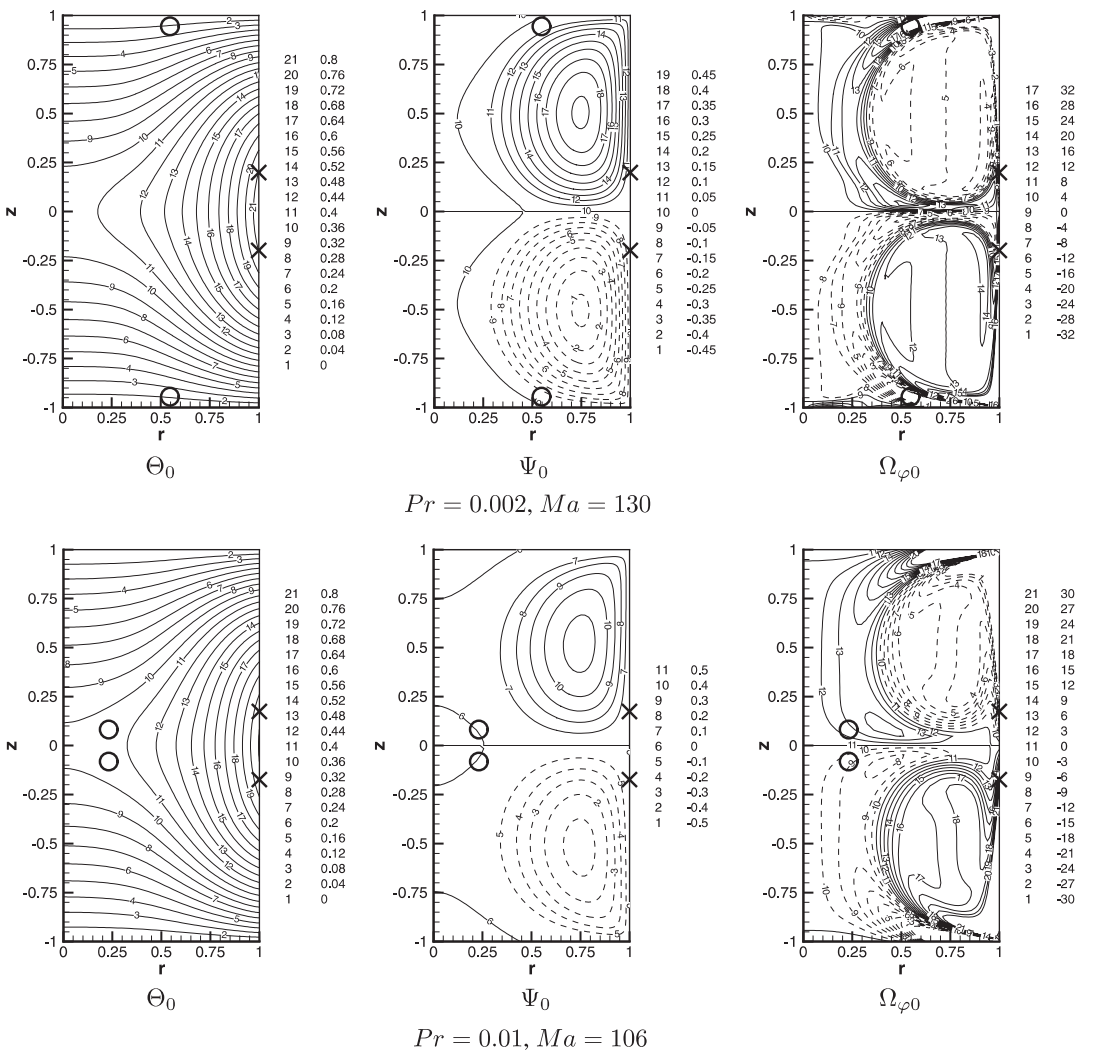

Figure 9. Temperature Θ_0, stream function Ψ_0 and vorticity $\Omega_{\varphi 0}$ of the stationary field $\mathbb{U}_0$. The crosses and circles indicate the points corresponding to the largest response to temperature and vorticity disturbances, respectively.

The sensitive location to disturbances in vorticity differs according to the transition type as shown in Figure 11. In the case of Hopf bifurcation, it is situated near the solid fronts in the vorticity tongue issued from the solid boundaries, while, in the case of pitchfork bifurcation, it is located at the heart of the liquid bridge near the zero iso-level of the stream function.

This difference between high and low flow regimes was argued by Kasperski *et al.* [30]. They demonstrated that the high-*Pr* instability is purely hydrothermal, while its origin is

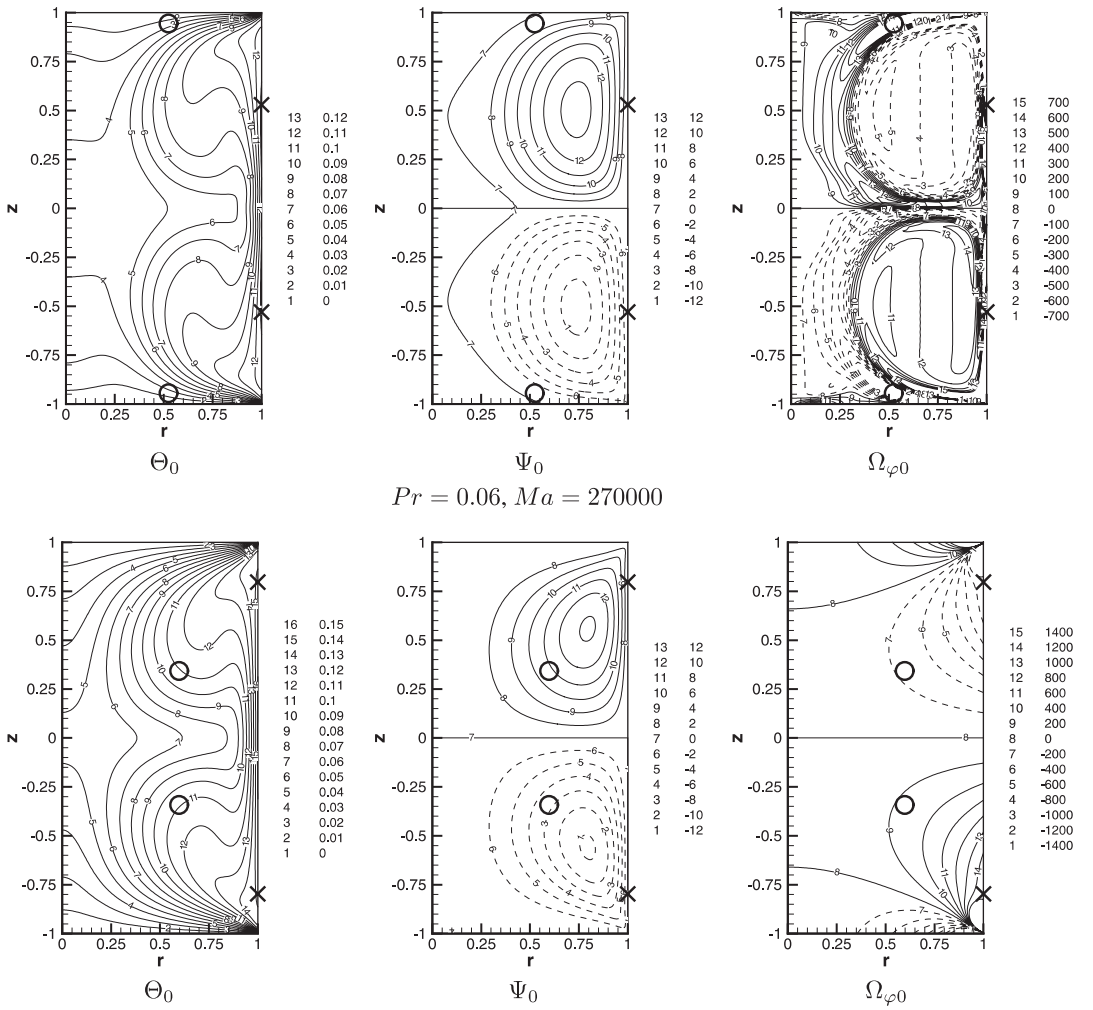

Figure 10. Temperature Θ_0, stream function Ψ_0 and vorticity $\Omega_{\varphi 0}$ of the stationary field $\mathbb{U}_0$. The crosses and circles indicate the points corresponding to the largest response to temperature and vorticity disturbances, respectively.

hydrodynamics in low-*Pr* flows. Referring to the above analysis of the stability map of Figure 2, the behaviour of the *Ma* stability thresholds with respect to the *Pr* values agrees with the thermal and hydrodynamic nature of the flow regime at $Pr > 1$ and $Pr < 1$, respectively. This was also confirmed with the evaluation of the kinetic and thermal energies balances [28]. The sensitivities at high *Pr* are in accordance with these results. At low *Pr* values, the sensitivity analysis of Hopf transitions exhibits the predominant part taken by the vorticity tongue advected from the solid surfaces. Previous works [19, 25] have proved the impact, on the global flow structure, of local scales, explicitly introduced by the vorticity singularity

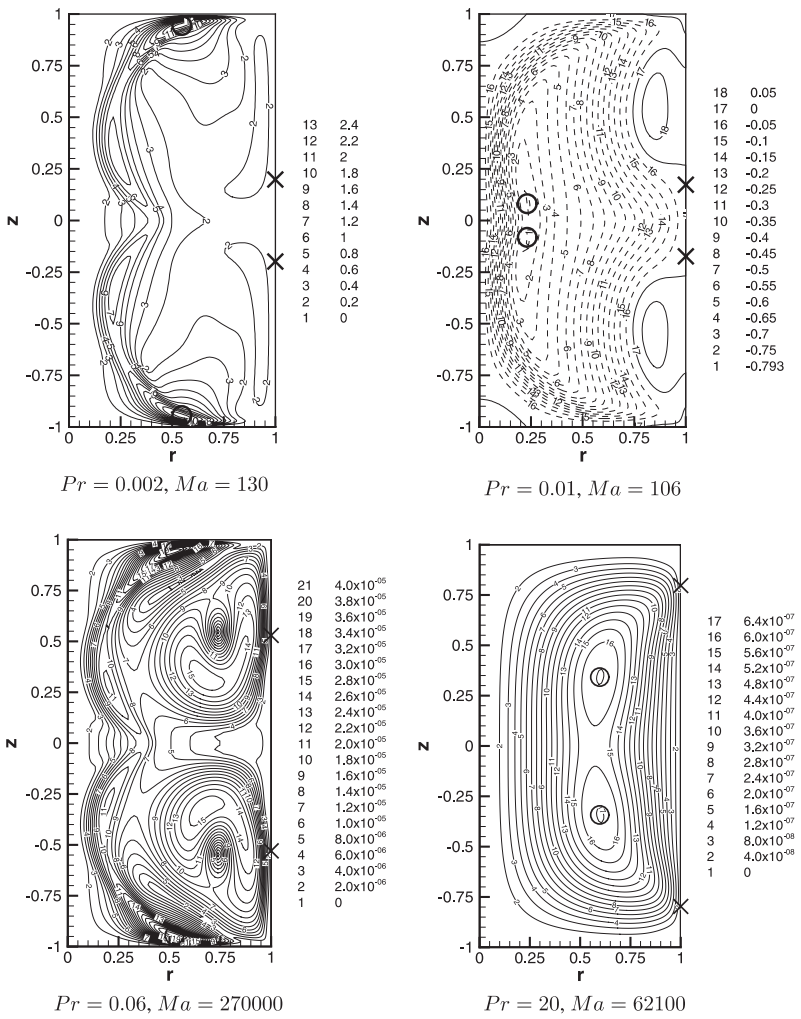

Figure 11. Adjoint stream function $\tilde{\psi}_1 r$. The circles indicate the points corresponding to the largest response to vorticity disturbance.

treatment at the junction of the free surface with the solid fronts. More surprising is the spatial sensitivity of the response to vorticity disturbance in case of pitchfork bifurcation.

6. APPLICATION TO THE FLOW CONTROL

As we have seen in the previous section, the most sensitive location, in case of temperature disturbance, is situated on the free surface. We will now explain how the method can help the experimenter to control stationary disturbance of the steady flow.

Suppose that we are in the vicinity of the parameter critical value and that the linear system approximation (20)–(21) is valid. Let us assume a time-dependent flow $\mathbb{U}(t)$, initially steady, which has lost its stability through a stationary bifurcation. This flow can be written as the linear superposition of the, both known, steady flow $\mathbb{U}_0$ and normalized leading stationary (i.e. λ_1 is real) perturbation $\mathbb{u}_1 e^{\lambda_1 t}$. Then, we can write

$$\mathbb{U}(r,z,t) = \mathbb{U}_0(r,z) + a_1 \mathbb{u}_1(r,z) \mathrm{e}^{\lambda_1 t} \tag{55}$$

In order to suppress the perturbation using a feedback control, we have to evaluate the coefficient a_1. Measuring, at time $t = t_m$ and at position (r_m, z_m), one component of the flow, for instance the temperature, we obtain

$$a_1 = \frac{\Theta(r_m, z_m, t_m) - \Theta_0(r_m, z_m, t_m)}{\theta_1(r_m, z_m) e^{\lambda_1 t_m}} \tag{56}$$

The way to restore the flow's stability is to apply an opposite perturbation, at time $t = t_s$, during a time step δt_s. For $t > t_s + \delta t_s$, Equation (55) then becomes

$$\mathbb{U}(r,z,t) = \mathbb{U}_0(r,z) + a_1 \mathbb{u}_1(r,z) \mathrm{e}^{\lambda_1 t} + \int_{t_s}^{t_s+\delta t_s} b_1(\tau) \mathbb{u}_1(r,z) \mathrm{e}^{\lambda_1 (t-\tau)} \, \mathrm{d}\tau \tag{57}$$

where b_1 is an unknown function.

Thus, $\mathbb{U}(r,z,t) = \mathbb{U}_0(r,z)$ only if

$$a_1 + \int_{t_s}^{t_s+\delta t_s} b_1(\tau) e^{-\lambda_1 \tau} \, \mathrm{d}\tau = 0 \tag{58}$$

The control applied by the experimenter has a spatial normalized shape $\mathbb{T}(r,z)$ and an amplitude ε, either depending or not on the time. Referring to Equation (14), the control perturbation is related to the function b_1 at time $t_s + \delta t_s$, by the equation

$$\int_{t_s}^{t_s+\delta t_s} (\varepsilon(\tau)\mathbb{T}, \tilde{\mathbb{u}}_1) \mathrm{e}^{\lambda_1 (t_s+\delta t_s-\tau)} \, \mathrm{d}\tau = \int_{t_s}^{t_s+\delta t_s} b_1(\tau) \mathrm{e}^{\lambda_1 (t_s+\delta t_s-\tau)} \, \mathrm{d}\tau \tag{59}$$

The amplitude $\varepsilon(t)$ can be chosen such that

$$\varepsilon(t) = \frac{b_1(t)}{(\mathbb{T}, \tilde{\mathbb{u}}_1)} \tag{60}$$

$b_1(t)$ being an arbitrary function provided it satisfies the integral relation (58).

Equation (60) exhibits that the amplitude is inversely proportional to the flow sensitivity to the control perturbation $\mathbb{T}$. It means that the higher the sensitivity of the flow to the applied control perturbation, the smaller the amplitude of the control perturbation.

7. CONCLUSION

We developed and validated a tool for computing sensitivity fields to linear perturbations of steady flows in the vicinity of bifurcation points. The sensitivity maps and, in particular, the

most sensitive loci to disturbances are directly related to the adjoint fields in case of disturbances at a local position. In case of Gaussian perturbations, they are obtained through inner products of the perturbations components with their related adjoint fields; the corresponding computing cost is negligible. The CPU cost and memory requirement to calculate, on the one hand, the leading adjoint eigenmode and, on the other hand, the time evolution of only one perturbation of the steady state are of the same order.

We applied the method to thermocapillary flows in liquid bridge submitted to a lateral heat flux. The associated adjoint linearized Navier–Stokes equations and boundary conditions were established.

In case of low Prandtl number values, strong sensitivity areas are situated on or near vorticity tongues, which are advected from the region near the junction of the free surface with the solid fronts, in agreement with the results published in References [19, 25].

We explained how an experimenter could apply the method to control the stationary instability of the thermocapillary flow by locally altering the temperature at optimal locations.

The extension of the method to the control of oscillatory perturbations and to the study of 3D perturbations should be straightforward.

ACKNOWLEDGEMENTS

This work has been performed with the computers of the IDRIS-CNRS and the CRI of the Université Paris-Sud XI and their helpful staff.

REFERENCES

1. Weisbin C, Peelle R, Marable J, Collins P, Kujawski E, Greenspan E, de Saussure G. Sensitivity and uncertainty analysis of reactor performance parameters. *Advances in Nuclear Science and Technology* 1982; **14**:247–312.
2. Jameson A, Pierce N, Martinelli L. Optimum aerodynamic design using the Navier–Stokes equations. *Theoretical and Computational Fluid Dynamics* 1998; **10**:213–237.
3. Baysal O, Eleshaky M. Aerodynamic sensitivity analysis-methods for the compressible Euler equations. *Journal of Fluids Engineering* 1991; **113**:681–688.
4. Cacuci D. Sensitivity theory for nonlinear systems. I. Nonlinear functional analysis approach. *Journal of Mathematical Physics* 1981; **22**(12):2794–2802.
5. Talagrand O, Courtier P. Variational assimilation of meteorological observations with the adjoint vorticity equation. I: theory. *Quarterly Journal of the Royal Meteorological Society* 1987; **113**:1311–1328.
6. V Jarny MO, Bardon J. A general optimization method using adjoint equation for solving multidimensional inverse heat conduction. *International Journal of Heat and Mass Transfer* 1991; **34**(11):2911–2919.
7. Lions J. *Optimal Control of Systems Governed by Partial Differential Equations*. Springer: Berlin, 1971.
8. Pironneau O. On optimum design in fluid mechanics. *Journal of Fluid Mechanics* 1974; **64**:97–110.
9. Jameson A. Aerodynamic design via control theory. *Journal on Scientific Computing* 1988; **3**:233–260.
10. Jameson A. Re-engineering the design process through computation. *Journal of Aircraft* 1999; **36**(1):36–50.
11. Giles M, Pierce N. Adjoint equations in CFD: duality, boundary conditions and solution behaviour. *AIAA Paper 97-1850*, 1997.
12. Giles M, Pierce N. On the properties of solutions of the adjoint Euler equations. *Numerical Methods for Fluid Dynamics VI. ICFD*, 1998.
13. Hill D. Adjoint systems and their role in the receptivity problem for boundary layers. *Journal of Fluid Mechanics* 1995; **292**:183–204.
14. Luchini P, Bottaro A. Görtler vortices: a backward-in-time approach to the receptivity problem. *Journal of Fluid Mechanics* 1998; **363**:1–23.
15. Luchini P, Bottaro A. Linear stability and receptivity analyses of the Stokes layer produced by an impulsively started plate. *Physics of Fluids* 2001; **13**(6):1668–1678.
16. Andersson P, Berggren M, Henningson D. Optimal disturbances and bypass transition in boundary layers. *Physics of Fluids* 1999; **11**(1):134–150.

17. Gadoin E, Le Quéré P, Daube O. A general methodology for investigating flow instabilities in complex geometries: application to natural convection in enclosures. *International Journal for Numerical Methods in Fluids* 2001; **37**:175–208.
18. Chénier E, Delcarte C, Labrosse G. Stability of the axisymmetric buoyant-capillary flows in a laterally heated liquid bridge. *Physics of Fluids* 1999; **11**(3):527–541.
19. Chénier E, Delcarte C, Kasperski G, Labrosse G. Sensitivity of the liquid bridge hydrodynamics to local capillary contributions. *Physics of Fluids* 2002; **14**:3109–3117.
20. Preisser F, Schwabe D, Scharmann A. Steady and oscillatory thermocapillary convection in liquid columns with free cylindrical surface. *Journal of Fluid Mechanics* 1983; **125**:545–567.
21. Shiomi J, Amberg G. Active control of a global thermocapillary instability. *Physics of Fluids* 2002; **14**(9): 3039–3045.
22. Roberts P. Characteristic value problems posed by differential equations arising in hydrodynamics and hydromagnetics. *Journal of Mathematical Analysis and Applications* 1960; **1**:195–214.
23. Giles M, Pierce N. An introduction to the adjoint approach to design. *Flow*, *Turbulence and Combustion* 2000; **65**:393–415.
24. Cröll A, Szofran F, Dold P, Benz K, Lehoczky S. Floating-zone growth of silicon in magnetic fields: II. Strong static axial fields. *Journal of Crystal Growth* 1998; **183**:554–563.
25. Chénier E, Delcarte C, Kasperski G, Labrosse G. *Interfacial Fluid Dynamics and Transport Processes*, Lecture notes in Physics, Chapter Thermocapillary flows and vorticity singularity, vol. 628. Springer: Heidelberg, 2003; 176–199.
26. Canuto C, Hussaini M, Quarteroni A, Zang T. *Spectral Methods in Fluid Dynamics*. Springer: Berlin, 1988.
27. Batoul A, Khallouf H, Labrosse G. Une méthode de résolution directe (pseudospectrale) du problème de Stokes 2D/3D instationnaire. Application à la cavité entrainée carrée. *Comptes Rendus de l'Académie des Sciences* 1994; **IIb**(319):1455–1461.
28. Bouizi O. Instabilités 3D de convection thermocapillaire en zone-flottante. *Ph.D. Thesis*, Université Paris-Sud XI, 2004.
29. Lehoucq R, Sorensen D, Yang C. *ARPACK Users Guide*, 1998.
30. Kasperski G, Batoul A, Labrosse G. Up to the unsteadiness of axisymmetric thermocapillary flows in a laterally heated liquid bridge. *Physics of Fluids* 2000; **12**(1):103–119.
31. Wanschura M, Shevtsova V, Kuhlmann H, Rath H. Convective instability mechanisms in thermocapillary liquid bridges. *Physics of Fluids* 1995; **7**(5):912–925.
32. Fjørtøft R. Application of integral theorems in deriving criteria of stability for laminar flows and for the baroclinic circular vortex. *Geofysiske Publikasjoner*, *Oslo* 1950; **17**(6):1–52.

